Quantum chaos of the Bose-Fermi Kondo model at intermediate temperature

Xinloong Han [1,*] and Zuodong Yu [2,3,†]

[1]*Department of Physics and HKU-UCAS Joint Institute for Theoretical and Computational Physics at Hong Kong,*
The University of Hong Kong, Hong Kong, China
[2]*Zhejiang Institute of Modern Physics and Department of Physics, Zhejiang University, Hangzhou, 310027, China*
[3]*Zhejiang Province Key Laboratory of Quantum Technology and Device, Zhejiang University, Hangzhou, 310027, China*

We study the quantum chaos in the Bose-Fermi Kondo model in which the impurity spin interacts with conduction electrons and a bosonic bath at the intermediate temperature in the large-N limit. The out-of-time-ordered correlator is calculated based on the Bethe-Salpeter equation and the Lyapunov exponent λ_L is extracted. Our calculation shows that the Lyapunov exponent monotonically increases as the Kondo coupling J_K increases, and it can reach an order of $\lambda_L \approx T$ as J_K approaches the multichannel Kondo fixed point (MCK). Furthermore, we also demonstrate that λ_L decreases monotonically as the impurity and bosonic bath coupling g increases, which is contrary to the general expectation that the most chaotic property occurs at the quantum critical point with the non-Fermi-liquid nature.

I. INTRODUCTION

Recently, the study of quantum chaos in many-body physics has drawn intensive interest [1–10]. Quantum chaos can be diagnosed by the so-called out-of-time-ordered correlators (OTOCs) [11,12]. The behavior of OTOCs has been investigated both theoretically and experimentally [13–20]. The OTOC was first introduced in the context of superconductivity [21] and then generalized to study information scrambling in a black hole close to the horizon. Usually, it is convenient to define the "regulated" OTOC [3,22–24],

$$\mathcal{C}(t) = \text{Tr}\{\sqrt{\rho}[\hat{W}(t), \hat{V}(0)]^\dagger \sqrt{\rho}[\hat{W}(t), \hat{V}(0)]\}, \quad (1)$$

where $\rho = e^{-\beta H}$ is the thermal density at the temperature $T = 1/\beta$. And $\hat{W}$ and $\hat{V}$ are local operators. In a chaotic system the OTOC is expected to have an exponential growth $C(t) \propto e^{\lambda_L t}$ at the intermediate time, where λ_L is called Lyapunov exponent. Under some reasonable conditions, the Lyapunov exponent λ_L is proven to have an upper bound $\lambda_L \leqslant 2\pi k_B T/\hbar$ [25] and saturates in the models with gravity duals. The most-celebrated $(0 + 1)D$ SYK$_4$ model with random all to all interactions [26–28] is a concrete example.

The Kondo model describes the systems in which the impurity spin strongly interacts with conduction electrons. Recently, the information scrambling in the two-channel and one-channel Kondo model has been investigated by mapping them onto the Majorana resonant level models [29]. Their results show that the OTOC for the impurity spin in the two-channel Kondo model is temperature independent and saturates to 1/4 at late time, while the OTOC in the one-channel Kondo model vanishes at late time, indicating

the absence of the butterfly effect. The Bose-Fermi Kondo model (BFKM) in which the impurity spin interacts with both conduction electrons and the bosonic bath, has rich physical properties, specially the non-Fermi-liquid state. From renormalization group (RG) analysis [30,31], it contains several nontrivial fixed points. At the low-temperature and -energy limit, a conformal symmetry can emerge at some fixed points. This model is an important system to study the dual of the gravity and many-body physics. Based on non-Fermi-liquid behavior and the emergent conformal symmetry, one may expect highly chaotic behavior in this model.

In this paper, we calculate the Lyapunov exponent in the BFKM in the large-N limit. Since the large-N treatment of BFKM gives the correct flow diagram and fixed point properties [31–34], our large-N calculation can capture the main physics of the BFKM. Our calculation shows that there are three types of diagrams which have the most important contributions to the OTOCs: two one-rung and one two-rung ladder diagrams. To extract the Lyapunov exponent λ_L from the Bethe-Salpeter equation, the equal-spaced discretization in the energy domain has to been taken. As a consequence of the shortcoming of the method, we can only study quantum chaos at the intermediate-temperature region instead of the low-temperature region $T \ll T_K^0$, where T_K^0 is the bare Kondo temperature. At the intermediate-temperature region we find that λ_T decreases monotonically as increasing temperature and the chaotic property will be lost at high temperature for a given J_K. Moreover, for fixed T and J_K, our numerical results show the chaotic properties are lost as the coupling between impurity and bosonic bath g increases, violating the expectation that the most chaotic behavior occurs at the quantum critical point with the non-Fermi-liquid nature.

The paper is organized as follows: In Sec. II, we introduce the BFKM in the large-N limit. In Sec. III, we use the Keldysh method to derive the self-consistent equations for Green's

*hanxinloong@gmail.com
†richzyu@gmail.com

functions and solve it with the help of fast-Fourier transformation method. In Sec. IV the OTOCs are calculated based on the Bethe-Salpeter equation in the large-N limit and the Lyapunov exponent is extracted from the OTOCs numerically. In Sec. V we show the results. Finally, we summarize the results and give conclusions in Sec. VI.

II. REVIEW OF THE BOSE-FERMI KONDO MODEL

The Bose-Fermi Kondo model is an effective model from the Kondo lattice problem in the extended dynamic mean-field theory [35–38] (EDMFT). The EDMFT reduces the lattice problem to an effective impurity problem, coupling to a fermionic bath and a bosonic bath. Then the Hamiltonian can be cast as

$$
\hat{H} = \sum_{k,\sigma,\alpha} E_k c_{k\sigma\alpha}^\dagger c_{k\sigma\alpha} + \sum_k \epsilon_k \Phi_k^\dagger \Phi_k
$$
$$
+ \frac{J_K}{N} \sum_{\alpha=1}^M \mathbf{S} \cdot \mathbf{s}_\alpha + \frac{g}{\sqrt{N}} \sum_k \mathbf{S} \cdot (\Phi_k + \Phi_k^\dagger), \quad (2)
$$

where $c_{k\sigma\alpha}^\dagger$ ($c_{k\sigma\alpha}$) is the creation (annihilation) operator of the conduction electron with channel index $\alpha = 1, \ldots, M$ and spin $\sigma = 1, \ldots, N$. The conduction electrons at the impurity site transform under the fundamental representation $\mathbf{s}_\alpha^i = \sum_{k\sigma\sigma'} c_{k\sigma\alpha}^\dagger \mathbf{t}_{\sigma\sigma'}^i c_{k\sigma'\alpha}$ ($i = 1, \ldots, N^2 - 1$) and couple to the impurity spin with interaction strength J_K. It is convenient to rewrite the impurity spin with N components pseudofermion f_α as $\mathbf{S}^i = \sum_{\sigma\sigma'} f_\sigma^\dagger S_{\sigma\sigma'}^i f_{\sigma'}$ by taking antisymmetric representation [30] with constraint $\sum_\sigma f_\sigma^\dagger f_\sigma = Q$ which can be absorbed into action by introducing the Lagrange multiplier μ. In this paper, we consider the case with particle-hole symmetry, requiring $Q = N/2$. g is the interaction strength with bosonic bath Φ_k with $N^2 - 1$ independent components which comes from the spin or magnetic fluctuation through Rudemam-Kittel-Kasuya-Yoshida exchange interaction [36,38] after generalizing the impurity spin from SU(2) to SU(N) symmetry. The ratio between M number and N is denoted as κ, which is taken as $\kappa = 1/2$ in the rest of the paper. The density of states of conduction electrons, $A_c(\omega)$, around Fermi surface can be approximately as $A_c(\omega) = \sum_k \delta(\omega - E_k) = \rho_0$ for $|\omega| < D/2$, where $D = 1/\rho_0$ is the bandwidth. The Greens' function for the bosonic bath in imaginary time is denoted as $\mathcal{G}_\Phi(\tau) \equiv -\langle \mathcal{T} \Phi(\tau) \Phi^\dagger(0) \rangle$. The bosonic spectrum $A_\Phi(\omega) = -\operatorname{Im} \mathcal{G}_\Phi(\omega + i\eta)/\pi = \sum_k [\delta(\omega - \epsilon_k) - \delta(\omega + \epsilon_k)]$ is considered as the sub-Ohmic bosonic spectrum, namely

$$
A_\Phi(\omega) = |\omega|^{1-\epsilon} \operatorname{sgn}(\omega), \quad (3)
$$

for $|\omega| < \Lambda$. And the parameter ϵ is at the range [0,1). In this paper we set $\hbar = 1$ and $k_B = 1$.

For the pure multichannel Kondo model, the previous study [30] proves there exists a nontrivial intermediate multichannel Kondo fixed point (*MCK*) between the trivial local moment fixed point *LM* and the strong-coupling limit $J_K \to \infty$ (see Fig. 1), and it hosts the conformal symmetry. When coupling to the bosonic bath, two other fixed points can appear [31]. One of them is the critical local moment point *LM′* and another one is the unstable critical fixed point *C*. The difference
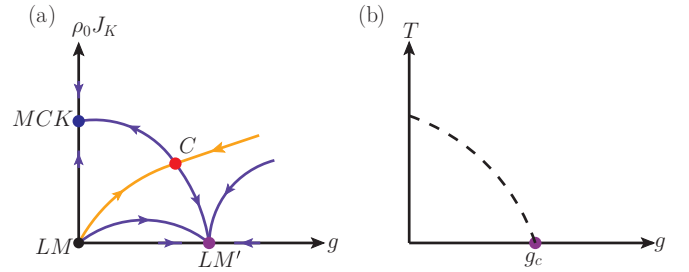

FIG. 1. The general RG flows and the phase transitions in the BFKM. (a) RG flows [30,31] in the parameter space $(g, \rho_0 J_K)$. Obviously, there exist three nontrivial fixed points, one unstable quantum critical fixed point C marked by the red point and a critical local moment fixed point LM' labeled by the purple point, and the last one, MCK, is related to the overscreened Kondo phase. The orange line is the line separating Kondo-singlet phase and the disorder phase. (b) The general phase diagram to describe the quantum phase transition. Here g_c denotes the quantum critical point.

of RG flows between the BFKM and the Kondo model leads to different chaotic behavior.

III. GREEN'S FUNCTIONS IN REAL TIME

To derive the Green's functions in real time, it is convenient to rewrite the model in the Keldysh time contour with backward and forward time evolution [39,40], which is denoted by the sign "−" and "+," respectively. Then the field ψ regardless of boson or fermion can be split into two parts as $\bar{\psi}(t) = (\bar{\psi}^+, \bar{\psi}^-)$ based on its causal position. After performing a Keldysh rotation [40], the Green's functions are written as

$$
\mathbf{G}_F = \begin{pmatrix} G_F^R & G_F^K \\ 0 & G_F^A \end{pmatrix}, \quad \mathbf{G}_B = \begin{pmatrix} G_B^K & G_B^R \\ G_B^A & 0 \end{pmatrix}, \quad (4)
$$

where R (A) represents the retarded (advanced) Green's function, respectively. The Keldysh part, which is denoted by K, is related to the retarded and advanced part by the fluctuation-dissipation theorem in the frequency domain,

$$
G_F^K(\omega) = \tanh\left(\frac{\omega}{2T}\right)[G_F^R(\omega) - G_F^A(\omega)], \quad (5)
$$
$$
G_B^K(\omega) = \coth\left(\frac{\omega}{2T}\right)[G_B^R(\omega) - G_B^A(\omega)]. \quad (6)
$$

Therefore, the noninteracting action can be written as

$$
S_0 = \int d\omega \Bigg\{ \sum_{\sigma\alpha} \sum_{\mathbf{k}} \Big[\bar{\Psi}_{\sigma\alpha}(\omega, \mathbf{k}) \mathbf{G}_c^{-1}(\omega, E_\mathbf{k}) \Psi_{\sigma\alpha}(\omega, \mathbf{k})
$$
$$
+ \sum_{\sigma'} \bar{\Phi}_{\sigma\sigma'}(\omega, \mathbf{k}) D_\Phi^{-1}(\omega, \epsilon_\mathbf{k}) \Phi_{\sigma\sigma'} \Big]
$$
$$
+ \sum_\sigma \bar{\mathcal{F}}_\sigma(\omega) \mathbf{G}_0^{-1}(\omega) \mathcal{F}_\sigma(\omega) \Bigg\}, \quad (7)
$$

where the fields is written in Keldysh space as $\bar{\Psi}_{\sigma\alpha}(\mathbf{k}) = (c_{1,\mathbf{k}\sigma\alpha}^\dagger, c_{2,\mathbf{k}\sigma\alpha}^\dagger)$, $\bar{\Phi}(\mathbf{k}) = (\Phi_{1,\mathbf{k}}^\dagger, \Phi_{2,\mathbf{k}}^\dagger)$, and $\bar{\mathcal{F}}_\sigma = (f_{1\sigma}^\dagger, f_{2\sigma}^\dagger)$.

The Green's function for conduction electrons and the bosonic bath are given by

$$G_c^R(\omega, \mathbf{k}) = \left[G_c^A(\omega, \mathbf{k})\right]^* = \frac{1}{\omega + i\eta - E_{\mathbf{k}}}, \quad (8)$$

$$D_\Phi^R(\omega, \mathbf{k}) = \left[D_\Phi^A(\omega, \mathbf{k})\right]^* = \sum_{s=\pm 1} \frac{s}{\omega + i\eta - s\epsilon_{\mathbf{k}}}, \quad (9)$$

and the bare Green's function for an impurity is given by

$$G_0^R(\omega) = \frac{1}{\omega + i\eta - \lambda}, \quad (10)$$

where λ is the saddle point of the Lagrangian multiplier to force the conservation of impurity electrons and it can be taken as zero because of the particle-hole symmetry $f_\sigma \leftrightarrow f_\sigma^\dagger$. For the interaction between the bosonic bath and impurities, the action is

$$S_{\Phi,\mathcal{F}} = \frac{-g}{\sqrt{2N}} \sum_{\sigma,\sigma'} \int dt \{\bar{\mathcal{F}}_\sigma(t)\gamma_1 \mathcal{F}_{\sigma'}(t)(\Phi_{1,\sigma\sigma'} + \bar{\Phi}_{1,\sigma\sigma'}) $$
$$+ \bar{\mathcal{F}}_\sigma(t)\gamma_2 \mathcal{F}_{\sigma'}(t)(\Phi_{2,\sigma\sigma'} + \bar{\Phi}_{2,\sigma\sigma'})\}. \quad (11)$$

For interaction between conduction electrons and impurities, we introduce M-flavor Hubbard-Stratonovich fields B_α, which leads to

$$S_{\Psi,\mathcal{B},\mathcal{F}}$$
$$= \frac{-1}{\sqrt{2N}} \sum_{\sigma,\alpha} \int dt \{\bar{\mathcal{F}}_\sigma \gamma_1 \Psi_{\sigma\alpha} B_{1\alpha} + \bar{\mathcal{F}}_\sigma \gamma_2 \Psi_{\sigma\alpha} B_{2\alpha} + \text{H.c.}\}$$
$$- \sum_\alpha \int d\omega \, \bar{\mathcal{B}}_\alpha \mathbf{D}_0^{-1}(\omega)\mathcal{B}_\alpha, \quad (12)$$

where $\bar{\mathcal{B}}_\alpha = (B_{1\alpha}^\dagger, B_{2\alpha}^\dagger)$. The matrix γ_1 and γ_2 are given as

$$\gamma_1 = \begin{pmatrix} 1 & 0 \\ 0 & 1 \end{pmatrix}, \quad \gamma_2 = \begin{pmatrix} 0 & 1 \\ 1 & 0 \end{pmatrix}, \quad (13)$$

and the bare propagator D_0 for B_α is

$$D_0^R(\omega) = \left[D_0^A(\omega)\right]^* = -\frac{1}{J_K}. \quad (14)$$

Therefore, the partition function is $\mathcal{Z} = \int \mathcal{D}[\Phi, \mathcal{F}, \mathcal{B}, \lambda]e^{i(S_0 + S_{\Phi,\mathcal{F}} + S_{\Psi,\mathcal{B},\mathcal{F}})}$. Due to interaction, the Green's functions will be renormalized and the self-energy for fermions or bosons has the following structure:

$$\boldsymbol{\Sigma}_F = \begin{pmatrix} \Sigma_F^R & \Sigma_F^K \\ 0 & \Sigma_F^A \end{pmatrix}, \quad \boldsymbol{\Sigma}_B = \begin{pmatrix} \Sigma_B^K & \Sigma_B^R \\ \Sigma_B^A & 0 \end{pmatrix}. \quad (15)$$

The self-energies are obtained by taking into account the most relevant Feynman diagrams in the large-N limit, shown in Fig. 2. Therefore, it is straightforward to obtain the following self-consistent equations (for more details, see Appendix A):

$$[G^R(\omega)]^{-1} = \omega - \lambda - \Sigma_a^R(\omega) - \Sigma_b^R(\omega), \quad (16)$$

$$i\Sigma_a^R(t) = \frac{g^2}{2}\left[D_\Phi^K(t)G^R(t) + D_\Phi^R(t)G^K(t)\right], \quad (17)$$

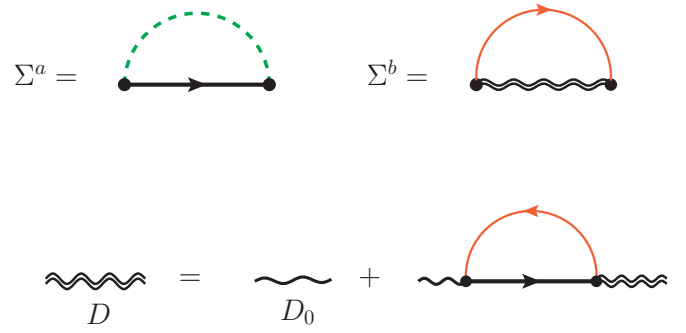$$i\Sigma_b^R(t) = \frac{\kappa}{2}\left[D^K(t)G_c^R(t) + D^R(t)G_c^K(t)\right], \quad (18)$$

FIG. 2. Feynman diagrams in the large-N limit. The black line represents the full impurity Green's function. Green dashed line is the bosonic bath propagator and red line denotes the propagator of the conduction electrons. The upper two diagrams are the self-energy corrections for the impurity fermions.

$$[D^R(\omega)]^{-1} = -1/J_K - \Pi^R(\omega), \quad (19)$$

$$i\Pi^R(t) = \frac{1}{2}\left[-G^K(-t)G_c^R(t) - G^A(-t)G_c^K(t)\right]. \quad (20)$$

Here $D_\Phi^R(t) = \int \frac{d\omega}{2\pi} D_\Phi^R(\omega)e^{i\omega t}$ and $G_c^R(t) = \int \frac{d\omega}{2\pi} G_c^R(\omega)e^{i\omega t}$. The Green's function for conduction electrons and the bosonic bath is obtained by using the Kramers-Kronig relation: $G_c^R(\omega) = \int d\omega' \frac{A_c(\omega')}{\omega + i\eta - \omega'}$ and $D_\Phi^R(\omega) = \int d\omega' \frac{A_\Phi(\omega')}{\omega + i\eta - \omega'}$.

To obtain the impurity and bosonic Green's functions, we numerically solve the self-consistent equations by the fast-Fourier transformation (FFT) method (for more details, see Appendix B). In practice, the electron spectrum is taken as a Gaussian function $A_c(\omega) = e^{-\omega^2/\pi}/\pi$. In Fig. 3, we plot the impurity and bosonic spectral functions respectively for different temperatures T and bosonic couplings g while fixing the Kondo coupling $J_K\pi/D = 1.0$. From Fig. 3, one can observe
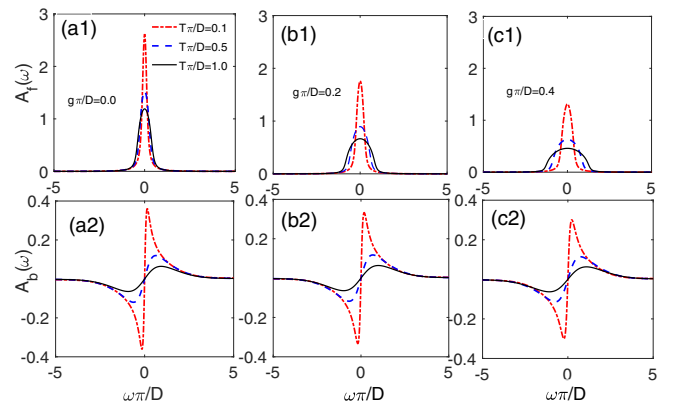

FIG. 3. The numerical results for the impurity spectral function $A_f(\omega) = -\text{Im}\, G^R(\omega)/\pi$ and bosonic spectral functions $A_b(\omega) = -\text{Im}\, D^R(\omega)/\pi$ at the fixed Kondo coupling $J_K\pi/D = 1.0$ and at the sub-Ohmic case $\epsilon = 0.5$. The red dash-dotted, blue dashed, and black solid lines correspond to the results at temperatures $T\pi/D = 0.1$, 0.5, and 1.0, respectively. Panels (a1), (a2), (b1), (b2), and (c1), (c2) are the spectral functions at the bosonic bath interaction $g\pi/D = 0$, 0.2, and 0.4, respectively.
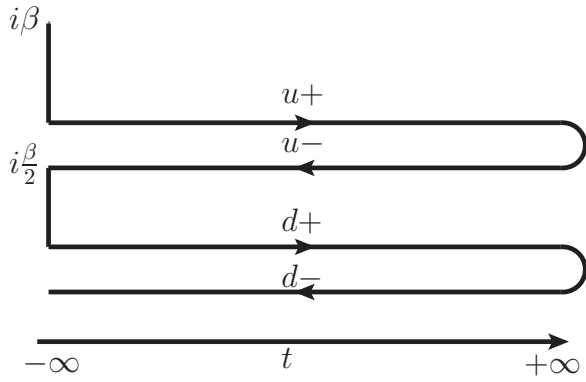
FIG. 4. The augmented Keldysh time contour for calculating the out-of-time-ordered correlators. The horizontal direction represents the real time evolution and the vertical direction represents the imaginary time evolution. It contains two Keldysh time contours, which are separated by $i\beta/2$ and labeled by u and d, respectively. Each Keldysh time contour contains two real-time evolutions, the forward one and the backward one.

amplitudes of impurity and bosonic spectral functions both decrease as increasing the bosonic bath coupling g.

IV. OUT-OF-TIME CORRELATOR AND BETHE-SALPETER EQUATION

It is convenient to evaluate the retarded "regulated" squared anticommutator defined as [3,22,24]

$$
\mathcal{C}(t_1, t_2) = \frac{\theta(t_1)\theta(t_2)}{N^2} \sum_{\sigma, \sigma'} \\
\times \mathrm{Tr}(\sqrt{\rho}\{f_\sigma(t_1), f_{\sigma'}^\dagger(0)\}\sqrt{\rho}\{f_\sigma(t_2), f_{\sigma'}^\dagger(0)\}^\dagger),
$$
(21)

where $\rho = \exp(-\beta H)$ is the thermal density matrix. It is clear that the OTO is defined in the two-copied Keldysh contours [4] separated by the imaginary time $i\beta/2$, as shown in Fig. 4. Here we denote each Keldysh contour with indices $s = (u, d)$. Therefore, the fermionic or bosonic field ψ in the two copied Keldysh contours is generalized to $\bar{\psi} = (\psi_{u,cl}^\dagger, \psi_{u,q}^\dagger, \psi_{d,cl}^\dagger, \psi_{d,q}^\dagger)$ after performing the Keldysh rotation for each time fold. Moreover the Green's function in each time fold remains the same, while the interloop Green's function $\mathbf{G}_{s\bar{s}}$ or $\mathbf{D}_{s\bar{s}}$ ($\bar{d} = u$ and $\bar{u} = d$) has the following structure:

$$
\mathbf{G}_{s\bar{s}} = \begin{pmatrix} 0 & G_{s\bar{s}}^K \\ 0 & 0 \end{pmatrix}, \quad \mathbf{D}_{s\bar{s}}(t) = \begin{pmatrix} D_{s\bar{s}}^K & 0 \\ 0 & 0 \end{pmatrix},
$$
(22)

where the component $G_{s\bar{s}}^K$ or $D_{s\bar{s}}^K$ follows the generalized fluctuation-dissipation theorem,

$$
G_{ud}^K(\omega) = \left[G_{du}^K(\omega)\right]^* = \frac{2i\,\mathrm{Im}\,G^R(\omega)}{\cosh\left(\frac{\omega}{2T}\right)},
$$
(23)

$$
D_{ud}^K(\omega) = D_{du}^K(\omega) = \frac{2i\,\mathrm{Im}\,D^R(\omega)}{\sinh\left(\frac{\omega}{2T}\right)}.
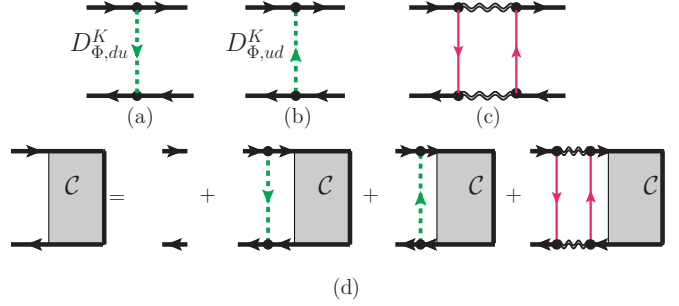$$
(24)

FIG. 5. Diagrammatically representations of the Bethe-Salpeter equations.

In the augmented Keldysh space, the OTO correlator $\mathcal{C}$ can be rewritten as

$$
\mathcal{C}(t_1, t_2) \\
= -\frac{\theta(t_1)\theta(t_2)}{N^2} \sum_{\sigma\sigma'} \langle f_\sigma^{d,cl}(t_1) \bar{f}_{\sigma'}^{d,cl}(0) \bar{f}_{\sigma'}^{u,q}(0) f_\sigma^{u,q}(t_2) \rangle_{aK},
$$
(25)

where $\langle \dots \rangle_{aK} = \int \mathcal{D}[\Phi, \mathcal{F}, \mathcal{B}, \lambda] e^{iS_{aK}}$ is the average in the augmented Keldysh contours. In large-N limit, vertex correction is ignored, so we use bare vertices in the Bethe-Salpeter equation, as illustrated in Fig. 5 to evaluate the quantum chaos in OTOC. The diagram contains two types of ladder diagrams, the first type are the two one-rung diagrams with Φ field connecting the up and down worlds, and the second type is the two-rung diagram with conduction electron fields linking the different worlds. Here are Feynman rules for these diagrams: (i) the rail lines in the upper world represents the advanced Green's functions, (ii) the rail lines sited in the down world are retarded Green's functions, (iii) the rungs connecting two worlds corresponds to the $G_{ud(du)}^K$ or $D_{ud(du)}^K$. Since there is no dissipation, time-translation symmetry holds. Hence we can take the following Fourier transformation:

$$
\mathcal{C}(t_1, t_2) = \frac{1}{N} \int \frac{d\Omega d\omega}{(2\pi)^2} e^{-i\Omega(t_1-t_2) - i\omega t} \mathcal{C}(\Omega, \omega),
$$
(26)

where we introduce the center-of-mass time separation $t = (t_1 + t_2)/2$. Following the aforementioned rules to calculate the OTOC, the zeroth order for $\mathcal{C}(\Omega, \omega)$ is

$$
\mathcal{C}_0(\Omega, \omega) = G^R\left(\Omega + \frac{\omega}{2}\right) G^A\left(\Omega - \frac{\omega}{2}\right) \equiv \mathcal{A}_\omega(\Omega), \quad (27)
$$

and $\mathcal{A}_\omega(\Omega)$ is a positive real number due to $G^R(\Omega + \omega/2) = [G^A(\Omega - \omega/2)]^*$. Summing up the ladder diagrams, we can obtain the Bethe-Salpeter equation,

$$
\mathcal{C}(\Omega, \omega) = \mathcal{A}_\omega(\Omega)\Big\{1 + \int \frac{d\Omega'}{2\pi} [\mathcal{K}_{1,\omega}(\Omega, \Omega') \\
+ \mathcal{K}_{2,\omega}(\Omega, \Omega')]\mathcal{C}(\Omega', \omega)\Big\},
$$
(28)

followed by the one-rung kernel $\mathcal{K}_{1,\omega}$,

$$
\mathcal{K}_{1,\omega} = \frac{ig^2}{2} D_{\Phi,ud}^K(\Omega' - \Omega) + \frac{ig^2}{2} D_{\Phi,du}^K(\Omega - \Omega'), \quad (29)
$$

and one two-rung kernel $\mathcal{K}_{2,\omega}$,

$$
\mathcal{K}_{2,\omega}(\Omega, \Omega') = \frac{\kappa}{4} \int \frac{d\omega'}{2\pi} \left[D^R\left(\omega' + \frac{\omega}{2}\right) \right.
$$
$$
\left. \times G^K_{c,ud}(\Omega - \omega') G^K_{c,du}(\Omega' - \omega') D^A\left(\omega' - \frac{\omega}{2}\right) \right].
$$
(30)

Finally, one can get the following ladder diagrams after dropping the irrelevant inhomogeneous term in Eq. (28):

$$
\mathcal{C}(\Omega, \omega) = \mathcal{A}_\omega(\Omega) \int \frac{d\Omega'}{2\pi} \bar{\mathcal{K}}_\omega(\Omega, \Omega') \mathcal{C}(\Omega', \omega). \quad (31)
$$

Here $\bar{\mathcal{K}}_\omega \equiv \mathcal{K}_{1,\omega} + \mathcal{K}_{2,\omega}$. We clarify that the above equation we obtained contains leading-order contributions in the large-N limit. While for finite N, the vertex correction might be relevant, especially for strong coupling, and one needs to take into account higher-order diagrams. The Lyapunov exponent λ_L corresponds to the positive solution of $-i\omega$ to make the integral kernel in the Bethe-Salpeter equation have a unit eigenvalue [23,41]. The existence of positive solution will signal the chaotic behavior, and on the other hand, it implies the absence of the chaotic properties. The details of the numerical calculation of Lyapunov exponent can be found in Appendix C.

V. NUMERICAL RESULTS

In this section, we give the numerical results of the Lyapunov exponent at the $O(1)$ order at the intermediate temperature in the large-N limit. From the Eqs. (30) and (31), it can be found that the eigenvalue λ_i of the kernel matrix $\mathcal{A}_\omega \mathcal{K}_\omega$ at $g = 0$ is proportional to the square of the Kondo coupling J_K at the weak-coupling limit, $\lambda_i \propto J_K^2$. Hence the condition for the existence of unit eigenvalues for a given $-i\omega$ cannot be satisfied because of $\lambda_i \propto J_K^2 \ll 1$, implying that there is no chaotic behavior at the weak-coupling limit for the pure multichannel Kondo model. This observation can be confirmed by the following numerical results:

In Fig. 6 we plot the ratio $\lambda_L/2\pi T$ as a function of temperature T at the fixed Kondo coupling $J_K\pi/D = 0.6$, $J_K\pi/D = 0.8$, $J_K\pi/D = 1.2$, and $J_K\pi/D = 1.5$ in the absence of coupling to the bosonic bath, $g = 0$. For a fixed J_k, the Lyapunov exponent always decreases monotonically as temperature increases. Furthermore, the chaotic behavior does not exist anymore when the temperature reaches a critical value, say T^*. One can expect this result because of its transition from non-Fermi-liquid character to the Fermi-liquid nature during the process of increasing temperature T. When the Kondo coupling J_K growths from the local moment fixed point (LM), it will reach the nontrivial overscreened multichannel fixed point (MCK) where the conformal symmetry will emerge [30]. One can also observe that the ratio λ_L/T grows monotonically upon reaching the MCK point, as shown in the Fig. 6, especially shown in the inset to Fig. 6 at $T\pi/D = 0.1$. $\lambda_L = 0$ at $J_K\pi/D \approx 0.21$ confirms our aforementioned analysis that the chaotic behavior vanishes at the weak-Kondo-coupling limit $J_K \ll 1$. One should note that the statement is obtained for finite temperature and is not
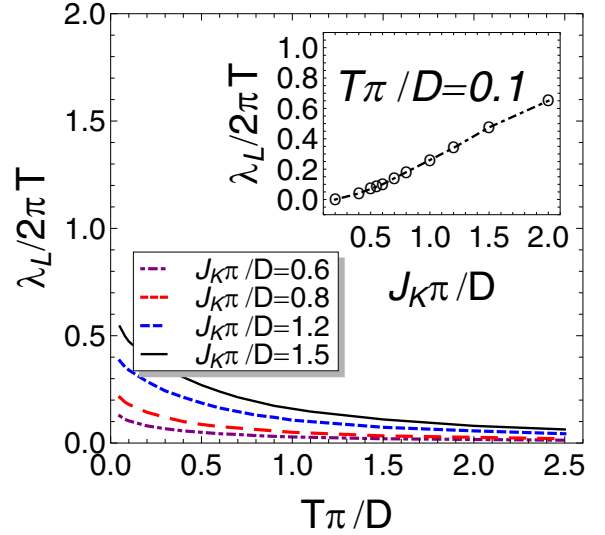

FIG. 6. $\lambda_L/2\pi T$ as a function of temperature $T\pi/D$ for the BKFM at $g\pi/D = 0$. The black solid, blue dashed, red dashed, and purple dot-dashed curves correspond to different Kondo couplings $J_K\pi/D = 1.5$, 1.2, 0.8, and 0.6. Inset shows $\lambda_L/2\pi T$ as a function of $J_K\pi/D$ for fixed temperature $T\pi/D = 0.1$. Here we fix $\kappa = \frac{M}{N} = 0.5$.

necessarily true for zero temperature when the scaling relation between Green's functions develops (see Appendix D).

Now we introduce the coupling between impurity and bosonic bath g. By increasing g, the systems will go through the overscreened multichannel Kondo phase to a critical local moment phase which is separated by a unstable fixed point [31,42,43,45,46] with critical coupling g_c. Generally, near the quantum critical point, the non-Fermi liquid develops and the conformal symmetry emerges, leading to the larger chaotic behavior with $\lambda_L \approx T$ than other regions away from the critical point [47]. To check this argument, we plot $\lambda_L/2\pi T$ as a function of temperature at different $g\pi/D$ and as a function of $g\pi/D$ at a fixed temperature $T\pi/D = 0.1$, as illustrated in Fig. 7. In Figs. 7(a) and 7(b) we obtain the two main observations: (1) For the sub-Ohmic case $\epsilon = 0.5$, the Lyapunov exponent decreases with growing bosonic coupling g for the same parameters (J_K, T). It shares the same behavior as the Ohmic case $\epsilon = 0$, although they have quiet different RG flows. This fact indicates the violation of the above argument. (2) The butterfly effect is stronger in the Ohmic case than in the sub-Ohmic case, as seen by comparing Fig. 7(a) with Fig. 7(b). To investigate the behavior of the Lyapunov exponent when crossing the critical point, we performed a detailed g-dependence calculation for various J_k at fixed temperature, as shown in Figs. 7(c) and 7(d). One can clearly see that the Lyapunov exponent is indeed monotonically decreasing with increasing g, and is finally vanishing at finite g. This monotonic behavior is consistent with the result that residual entropy for this model increases monotonically from the MCK phase to LM' phase [45]. For a conformal invariance system, the g theorem predicts that entropy should decrease along RG trajectories, which leads to a maximum value of entropy at the critical point and similarly also the largest chaotic behavior. The behavior of residual entropy in the
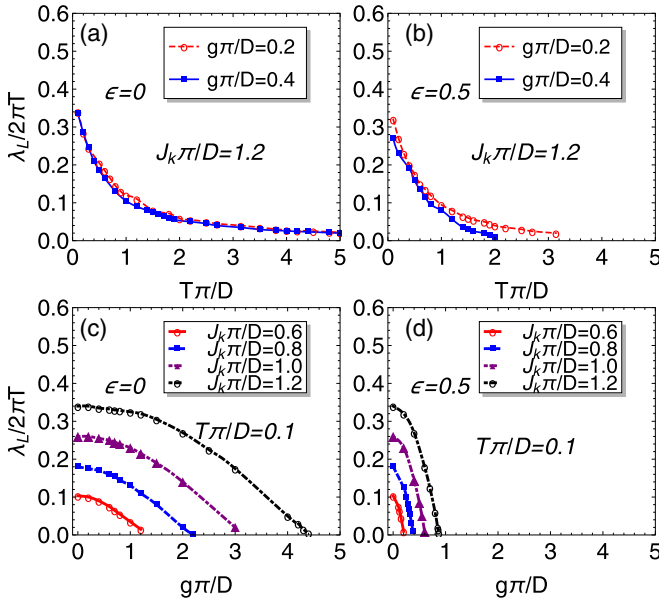
FIG. 7. The ratio $\lambda_L/2\pi T$ as a function of (a), (b) temperature $T\pi/D$ and as a function of (c), (d) bosonic coupling g. Here we fix $\kappa = 0.5$.

sub-Ohmic case is quite different from conformal invariance system due to its breaking of conformal symmetry. From numerical perspective, the reason of the decreasing of λ_L with g can be attributed to the suppressive effect of the magnitude of spectral functions of impurity and auxiliary bosons, as shown in Fig. 3.

VI. CONCLUSIONS

In this paper, we derive the Bethe-Salpeter equation for our defined impurity OTO correlator for BFKM in large-N limit. We find that the biggest contribution comes from two one-rung and one two-rung diagrams whose up and down world lines are connected by the bosonic bath and the conduction electrons, respectively. The numerical calculation at the intermediate temperature shows that the Lyapunov exponent λ_L decreases with increasing temperature and finally vanishes at a finite temperature, which depends on the one- and two-channel Kondo models in which the impurity OTOC is temperature-independent. We also observe that the system has no butterfly effect below a typical Kondo coupling J_K

for finite temperature. When coupled to the bosonic bath, the monotonic decrease of λ_L does not obey the general argument that the highest chaotic behavior occurs at the quantum critical point but is consistent with the behavior of impurity entropy and is due to breaking conformal invariance in the model [45].

APPENDIX A: SELF-CONSISTENT EQUATIONS AND DIAGRAMS FOR OUT-OF-TIME-ORDERED CORRELATOR

The action for the impurity and bosonic bath in the Keldysh contour $\mathcal{C}$ is given by

$$
\begin{aligned}
S_{\Phi,f} &= \frac{-g}{\sqrt{N}} \sum_{\sigma\sigma'} \int_{\mathcal{C}} dt\, f_\sigma^\dagger(t) f_{\sigma'}(t) [\Phi_{\sigma\sigma'}(t) + \Phi_{\sigma\sigma'}^\dagger(t)], \\
&= \frac{-g}{\sqrt{N}} \sum_{\sigma\sigma'} \sum_{s=\pm} \int_{-\infty}^{+\infty} dt\, s f_{s,\sigma}^\dagger(t) f_{s,\sigma'}(t) \\
&\quad \times [\Phi_{s,\sigma\sigma'}(t) + \Phi_{s,\sigma\sigma'}^\dagger(t)],
\end{aligned}
\tag{A1}
$$

where $s = \pm$ denote the forward (backward) branch in the Keldysh contour. It is useful to make the following Keldysh rotation for fermionic fields:

$$
f_1 = \frac{1}{\sqrt{2}}(f_+ + f_-), \quad f_2 = \frac{1}{\sqrt{2}}(f_+ - f_-), \tag{A2}
$$

$$
\bar{f}_1 = \frac{1}{\sqrt{2}}(\bar{f}_+ - \bar{f}_-), \quad \bar{f}_2 = \frac{1}{\sqrt{2}}(\bar{f}_+ + \bar{f}_-), \tag{A3}
$$

and bosonic fields:

$$
\Phi_1 = \frac{1}{\sqrt{2}}(\Phi_+ + \Phi_-), \quad \Phi_2 = \frac{1}{\sqrt{2}}(\Phi_+ - \Phi_-), \tag{A4}
$$

$$
\bar{\Phi}_1 = \frac{1}{\sqrt{2}}(\bar{\Phi}_+ + \bar{\Phi}_-), \quad \bar{\Phi}_2 = \frac{1}{\sqrt{2}}(\bar{\Phi}_+ - \bar{\Phi}_-). \tag{A5}
$$

Then after Keldysh rotation, the action becomes

$$
S_{\Phi,f} = \frac{-g}{\sqrt{2N}} \sum_{\sigma\sigma'} \int dt\{(\bar{f}_{1,\sigma}f_{2,\sigma'} + \bar{f}_{2,\sigma}f_{1,\sigma'})(\bar{\Phi}_{2,\sigma\sigma'} + \Phi_{2,\sigma\sigma'}) + (\bar{f}_{1,\sigma}f_{1,\sigma'} + \bar{f}_{2,\sigma}f_{2,\sigma'})(\bar{\Phi}_{1,\sigma\sigma'} + \Phi_{1,\sigma\sigma'})\}. \tag{A6}
$$

We can write the action into a compact form by taking $\bar{\mathcal{F}}_\sigma = (\bar{f}_{1,\sigma}, \bar{f}_{2,\sigma})$, leading to Eq. (11). After the Hubbard-Stratonovich transformation, one can obtain

$$
S_{c,B,f} = -\int_{\mathcal{C}} dt \left\{ \sum_{\alpha\sigma} \left[\frac{1}{\sqrt{N}} f_\sigma^\dagger(t) c_{\sigma\alpha}(t,\mathbf{0}) B_\alpha(t) + \frac{1}{\sqrt{N}} c_{\sigma\alpha}^\dagger(t,\mathbf{0}) f_\sigma(t) B_\alpha^\dagger(t) \right] - \sum_\alpha \frac{B_\alpha^\dagger(t) B_\alpha(t)}{J_K} \right\}, \tag{A7}
$$

then after Keldysh rotation, we obtain Eq. (12). In the large-N limit($N \to +\infty$), only Feynman diagrams as shown in Fig. 2 can contribute to the self-energies for propagators of impurity fermions f and bosonic fields B. Thus we can write the retarded

Green's function $iG^R(t) = \langle f_{1\sigma}(t)\bar{f}_{1\sigma}(0)\rangle_M$ as

$$
\langle f_{1\sigma}(t)\bar{f}_{1\sigma}(0)\rangle_M = \langle f_{1\sigma}(t)f_{1\sigma}^\dagger(0)\rangle_0 + \frac{g^2}{2N}\int dt_1 dt_2 \langle f_{1\sigma}(t)
$$

$$
\times \sum_{\sigma_1,..,\sigma_4} \left\{ (\bar{f}_{1\sigma_1}f_{2\sigma_2} + \bar{f}_{2\sigma_1}f_{1\sigma_2})(\Phi_{2\sigma_1\sigma_2} + \bar{\Phi}_{2\sigma_1\sigma_2}) + (\bar{f}_{1\sigma_1}f_{1\sigma_2} + \bar{f}_{2\sigma_1}f_{2\sigma_2})(\Phi_{1\sigma_1\sigma_2} + \bar{\Phi}_{1\sigma_1\sigma_2}) \right\}_{t_1}
$$

$$
\times \left\{ (\bar{f}_{1\sigma_3}f_{2\sigma_4} + \bar{f}_{2\sigma_3}f_{1\sigma_4})(\Phi_{2\sigma_3\sigma_4} + \bar{\Phi}_{2\sigma_3\sigma_4}) + (\bar{f}_{1\sigma_3}f_{1\sigma_4} + \bar{f}_{2\sigma_3}f_{2\sigma_4})(\Phi_{1\sigma_3\sigma_4} + \bar{\Phi}_{1\sigma_3\sigma_4}) \right\}_{t_2} \bar{f}_\sigma(0)\rangle_M
$$

$$
+ \frac{1}{2N} \sum_{\alpha,\sigma_1,\sigma_2} \int dt_1 dt_2 \langle f_{1\sigma}(t)\left\{ \bar{f}_{1\sigma_1}c_{2\sigma_1\alpha}B_{2\alpha} + \bar{f}_{2\sigma_1}c_{1\sigma_1\alpha}B_{2\alpha} + \bar{f}_{1\sigma_1}c_{1\sigma_1\alpha}B_{1\alpha} + \bar{f}_{2\sigma_1}c_{2\sigma_1}B_{1\alpha} \right\}_{t_1}
$$

$$
\times \left\{ \bar{c}_{1\sigma_2\alpha}f_{1\sigma_2}\bar{B}_{1\alpha} + \bar{c}_{2\sigma_2\alpha}f_{2\sigma_2}\bar{B}_{1\alpha} + \bar{c}_{2\sigma_2\alpha}f_{1\sigma_2}\bar{B}_{2\alpha} + \bar{c}_{1\sigma_2\alpha}f_{2\sigma_2}\bar{B}_{2\alpha} \right\}_{t_2} \bar{f}_{1\sigma}(0)\rangle_M, \tag{A8}
$$

where $\langle\rangle_M$ means the expectation in the many-body ground state, and $\{\bar{f}cB\}_t = \{\bar{f}(t)c(t)B(t)\}$. It is straightforward to obtain

$$
iG^R(t) = iG_0^R(t) + \int dt_1 dt_2 [iG_0^R(t - t_1)]
$$

$$
\times \left\{ \frac{g^2}{2N} \sum_{\sigma_3 = \sigma_4} \left\{ [iG^K(t_1 - t_2)][iD_\Phi^R(t_1 - t_2)] + [iG^R(t_1 - t_2)] \right. \right.
$$

$$
\times [iD_\Phi^K(t_1 - t_2)] \right\} + \frac{1}{2N} \sum_\alpha \left\{ [iG_c^K(t_1 - t_2)][iD^R(t_1 - t_2)] + [iG_c^R(t_1 - t_2)] \right.
$$

$$
\left. \left. \times [iD^K(t_1 - t_2)] \right\} \right\} [iG^R(t_2)], \tag{A9}
$$

by using the structure of Green's functions and causality of $G^R(t)D^A(t) = 0$. By defining the self-energies for impurity fermions as Eqs. (17) and (18), one can obtain

$$
iG^R(t) = iG_0^R(t) - \int dt_1 dt_2 iG_0^R(t - t_1)[i\Sigma_a^R(t_1 - t_2) + i\Sigma_b^R(t_1 - t_2)]iG^R(t_2), \tag{A10}
$$

after doing Fourier transformation, one can obtain the Eq. (16). Using the same method, one can also derive Eqs. (19) and (20). After Keldysh rotation, the OTOC is

$$
\mathcal{C}(t_1, t_2) = -\frac{\theta(t_1)\theta(t_2)}{N^2} \sum_{\sigma\sigma'} \langle f_\sigma^{d,cl}(t_1)\bar{f}_{\sigma'}^{d,cl}(0)\bar{f}_{\sigma'}^{u,q}(0)f_\sigma^{u,q}(t_2)\rangle_{aK} \tag{A11}
$$

in the zeroth order, so it can be reduced to

$$
\mathcal{C}_0(t_1, t_2) = -\frac{\theta(t_1)\theta(t_2)}{N^2} \sum_{\sigma\sigma'} \langle f_\sigma^{d,cl}(t_1)\bar{f}_{\sigma'}^{d,cl}(0)\rangle_0 \langle \bar{f}_{\sigma'}^{u,q}(0)f_\sigma^{u,q}(t_2)\rangle_0 = \frac{\theta(t_1)\theta(t_2)}{N} G_0^R(t_1, 0)[G_0^R(t_2, 0)]^*. \tag{A12}
$$

In the Feynman diagrams (see Fig. 8), the zeroth order can be represented by the upper (lower) lines which is the retarded (advanced) Green's function. After considering the interactions, the retarded (advanced) Green's function will be renormalized by the self-energies which contains the Keldysh part of the Green's function in Keldysh space, as shown in the main text for self-consistent equations for Green's functions. Generally, we can count the order of Feynman diagrams based on the following rules: (1) The Green's function on the upper(lower) real-time fold is the restarted (advanced) Green's function. (2) The Green's function connecting the upper and lower real time fold is the Wightman function. (3) Each vertex insertion is on the order of $1/\sqrt{N}$. (4) The interaction between the bosonic field B_α impurity fermions f_σ is through the term $B_\alpha \bar{f}_\sigma c_{\sigma\alpha}$ or $\bar{B}_\alpha \bar{c}_{\sigma\alpha}f_\sigma$. (5) The interaction between the bosonic bath Φ and the impurity fermions f_σ is through the term $\bar{f}_\sigma f_{\sigma'}(\Phi_{\sigma\sigma'} + \bar{\Phi}_{\sigma\sigma'})$. (6) The correlation function for the bosonic bath is $\langle \mathcal{T}\Phi_{\sigma\sigma'}\Phi_{\sigma_1\sigma_2}^\dagger \rangle \propto \delta_{\sigma\sigma_1}\delta_{\sigma'\sigma_2}$. (7) The correlation function for the fermionic bath is $\langle \mathcal{T}c_{\alpha\sigma}c_{\beta\sigma'}^\dagger \rangle \propto \delta_{\alpha,\beta}\delta_{\sigma\sigma'}$. In the derivation of the OTOC, we restrict the vertex insertions only in real-time folds because the vertex insertions along the thermal circle do not directly lead to time growth [3].

The subleading-order diagrams (see Fig. 9) in the calculation of the Bethe-Salpeter equations will vanish in the limit $N = \infty$. Therefore, in this large-N limit, our Bethe-Salpeter equation Eq. (31) in the main text is an exact result.

APPENDIX B: NUMERICAL TECHNIQUE TO SOLVE THE SADDLE-POINT EQUATIONS

Since the calculation of the Lyapunov exponent requires the equal spacing $\Delta\omega$ in the frequency domain, the Fourier transformation method is used to solve the self-consistent equations (16) and integral kernel $\mathcal{A}_\omega \mathcal{K}_\omega$ in the main text. Since we have the relation $\Delta\omega \propto \frac{1}{N_t} \leqslant T$ where N_t is the total points, to get accurate calculations, we need a huge number of data points, which is beyond our computational resources. We
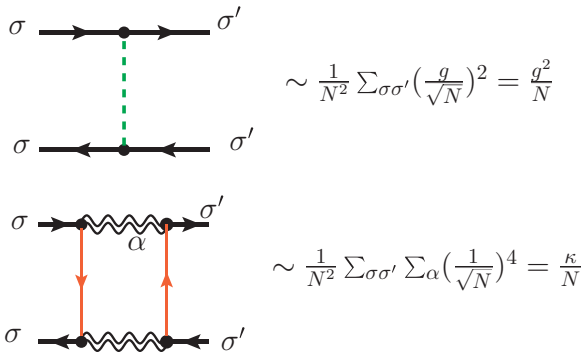
FIG. 8. Feynman diagrams for the Bethe-Salpeter equation. (a) The leading-order Feynman diagram with one rung of the bosonic bath. (b) Feynman diagrams with two rungs of the fermion bath.

discretize the frequency and time domain as

$$\Omega_d = \frac{2\pi f_s}{N_t}\left[\frac{1-N_t}{2}, \frac{3-N_t}{2}, \ldots, \frac{N_t-3}{2}, \frac{N_t-1}{2}\right], \quad (B1)$$

$$T_d = \frac{1}{f_s}\left[\frac{1-N_t}{2}, \frac{3-N_t}{2}, \ldots, \frac{N_t-3}{2}, \frac{N_t-1}{2}\right]. \quad (B2)$$

The Fourier transformation $G(t) = \int \frac{d\omega}{2\pi} G(\omega) e^{-i\omega t}$ and $G(\omega) = \int_0^{+\infty} dt\, G(\omega) e^{i\omega t}$ for Green's functions can be performed by the FFT algorithm. We iteratively solve the equations and obtain the self-consistent solutions if the error $\max(|G(\omega) - \bar{G}(\omega)|)$ where G and $\bar{G}$ belong to two nearest iterative steps is less than 10^{-6}. In practice, the total point $N_t = 2^{21} + 1$ and $f_s = 4$ is used. The cutoff for the frequency is $\omega_c = 4\pi$ which is four times of bandwidth D. In our numerical calculations the spectral function of the bosonic bath is taken as

$$A_\Phi(\omega) = \begin{cases} |\omega|^{1-\epsilon}\,\mathrm{sgn}(\omega), & |\omega| < \Lambda \\ |\Lambda|^{1-\epsilon}\,\mathrm{sgn}(\omega)e^{-c(|\omega|-\Lambda)}, & |\omega| \geqslant \Lambda, \end{cases} \quad (B3)$$

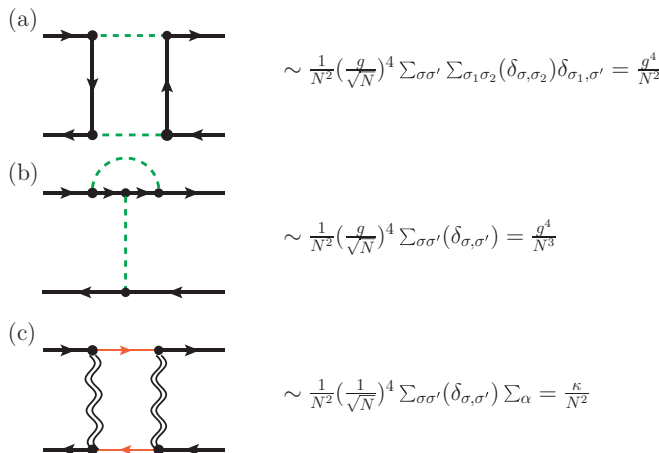where energy cutoff $\Lambda = 0.05$ and $c = 15$.

FIG. 9. Some subleading-order diagrams for the Bethe-Salpeter equations.

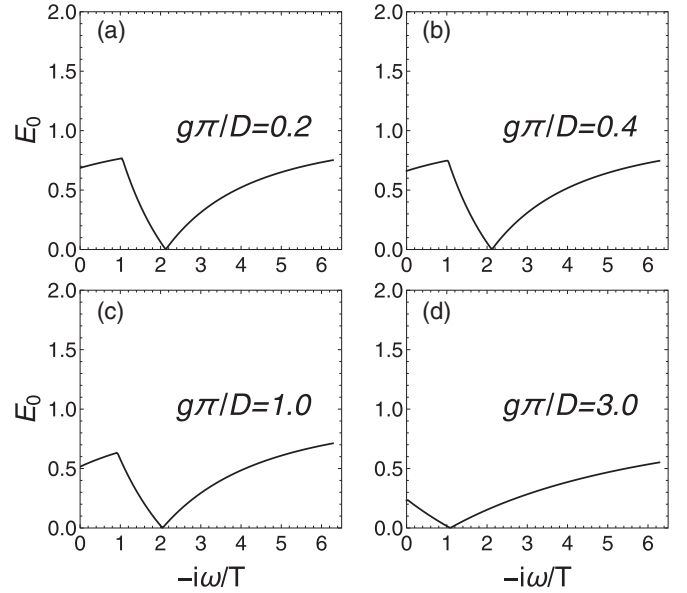FIG. 10. Plot of the magnitude of E_0 as a function of $-i\omega/T$ in the positive axis at the given $J_K\pi/D = 1.2$ for (a) $g\pi/ = 0.2$, (b) 0.4, (c) 1.0, and (d) 3.0.

APPENDIX C: NUMERICAL METHOD FOR THE LYAPUNOV EXPONENT

To numerically calculate the Lyapunov exponent, we first discretize the frequency to transform the integral equation into a linear algebra equation where the integral kernel $\mathcal{A}_\omega(\Omega)\mathcal{K}_\omega(\Omega, \Omega')$ becomes a matrix. The Lyapunov exponent corresponds to the positive value $-i\omega$ which leads to the existence of a unit eigenvalue of the kernel matrix. Here the energy is discretized in range $(-5, 5)$ with total number $N_{size} = 800$. The consistency of the result for N_{size} is checked with a smaller interval. In Fig. 10, we illustrates the evolution of $E_0 = \min|1 - \lambda_i|$ where λ_i is the eigenvalue of the integral kernel of the Bethe-Salpeter equation Eq. (31). Based on our numerical calculations, we plot the general phase diagrams for the chaotic and nonchaotic regions as shown in Fig. 11.
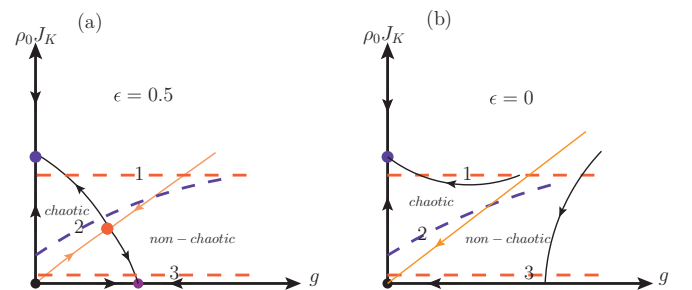

FIG. 11. The general phase diagram for the chaotic and nonchaotic phase with the RG flow diagram for the (a) sub-Ohmic $\epsilon = 0.5$ case and (b) Ohmic case [44] $\epsilon = 0$. Our data covers the region between the red dashed line 1 and 3. The blue dashed line separates the chaotic and nonchaotic regions for a given intermediate temperature.

APPENDIX D: BETHE-SALPETER EQUATION AT THE LOW-TEMPERATURE LIMIT

Argument in the main text that $\lambda_i \propto J_K^2$ at the intermediate temperature in the absence of bosonic bath cannot be applied to the case at the low-temperature limit. For the $g = 0$ case, the flow diagram tells us that the system will flow to the *MCK* point at any finite J_K. Then we can apply the scaling ansatz:

$$\text{Im}\, G(\omega) = -M_f |\omega|^{\alpha_f - 1}, \tag{D1}$$

$$\text{Im}\, D(\omega) = -M_B |\omega|^{\alpha_B - 1} \tag{D2}$$

for fixed-point Green's functions at zero temperature [30]. Inserting these relations into self-consistent equations, one can obtain the relation for amplitudes and exponents:

$$\alpha_f = 1 - \alpha_B = \frac{1}{1 + \kappa}, \tag{D3}$$

$$M_c M_f M_B \propto \alpha_f \tan\left(\frac{\pi \alpha_f}{2}\right) \tag{D4}$$

for the *MCK* fixed point at $g = 0$. M_c is the amplitudes prefactor for conduction electrons. This means that, at zero temperature, the solution of the Bethe-Salpeter equation (28) does not dependent on the value of J_K, i.e., the eigenvalue λ_i should saturate to the same value for any finite J_K, similar to the entropy results [45].

[1] B. Swingle and T. Senthil, Phys. Rev. B **87**, 045123 (2013).
[2] S. Sachdev, Phys. Rev. X **5**, 041025 (2015).
[3] D. Chowdhury and B. Swingle, Phys. Rev. D **96**, 065005 (2017).
[4] Igor L. Aleiner, L. Faoro, and Lev B. Ioffe, Ann. Phys. (NY) **375**, 378 (2016).
[5] X. Y. Song, C. M. Jian, and L. Balents, Phys. Rev. Lett. **119**, 216601 (2017).
[6] S. Banerjee and E. Altman, Phys. Rev. B **95**, 134302 (2017).
[7] S. A. Hartnoll, A. Lucas, and S. Sachdev, *Holographic Quantum Matter* (The MIT Press, 2018).
[8] B. Swingle, Nat. Phys. **14**, 988 (2018).
[9] X. Han and B. Liu, Phys. Rev. B **102**, 045123 (2020).
[10] D. Stanford, J. High Energy Phys. 10 (2016) 009.
[11] S. H. Shenker and D. Stanford, J. High Energy Phys. 03 (2014) 067.
[12] A. Kitaev, Hidden correlations in the Hawking radiation and thermal noise, *talk given at Fundamental Physics Prize Symposium, in Proceedings of the Stanford SITP seminars* (2014).
[13] M. Rigol, V. Dunjko, and M. Olshanii, Nature (London) **452**, 854 (2008).
[14] T. Langen, R. Geiger, M. Kuhnert, B. Rauer, and J. Schmiedmayer, Nat. Phys. **9**, 640 (2013).
[15] A. M. Kaufman, M. E. Tai, A. Lukin, M. Rispoli, R. Schittko, P. M. Preiss, and M. Greiner, Science **353**, 794 (2016).
[16] G. Zhu, M. Hafezi, and T. Grover, Phys. Rev. A **94**, 062329 (2016).
[17] N. Y. Yao, F. Grusdt, B. Swingle, M. D. Lukin, D. M. Stamper-Kurn, J. E. Moore, and E. Demler, arXiv:1607.01801.
[18] G. Bentsen, T. Hashizume, A. S. Buyskikh, E. J. Davis, A. J. Daley, S. S. Gubser, and M. Schleier-Smith, Phys. Rev. Lett. **123**, 130601 (2019).
[19] M. Gättner, J. G. Bohnet, A. Safavi-Naini, M. L. Wall, J. J. Bollinger, and A. M. Rey, Nat. Phys. **13**, 781 (2017).
[20] C. B. Dağ and L.-M. Duan, Phys. Rev. A **99**, 052322 (2019).
[21] A. I. Larkin, and Y. N. Ovchinnikov, J. Exp. Theor. Phys. **28**, 1200 (1969).
[22] Markus J. Klug, Mathias S. Scheurer, and Jörg Schmalian, Phys. Rev. B **98**, 045102 (2018).
[23] A. A. Patel and S. Sachdev, Proc. Natl. Acad. Sci. USA **114**, 1844 (2017).
[24] S. Jian and H. Yao, arXiv:1805.12299.
[25] J. Maldacena, S. H. Shenker, and D. Stanford, J. High Energy Phys. 08 (2016) 106.
[26] S. Sachdev and J. Ye, Phys. Rev. Lett. **70**, 3339 (1993).
[27] A. Kitaev, A simple model of quantum holography; KITP http://online.kitp.ucsb.edu/online/entangled15/kitaev/ (2015).
[28] J. Maldacena and D. Stanford, Phys. Rev. D **94**, 106002 (2016).
[29] B. Dóra, M. A. Werner, and C. P. Moca, Phys. Rev. B **96**, 155116 (2017).
[30] O. Parcollet, A. Georges, G. Kotliar, and A. Sengupta, Phys. Rev. B **58**, 3794 (1998).
[31] L. Zhu and Q. Si, Phys. Rev. B **66**, 024426 (2002).
[32] M. Vojta and M. Kircan, Phys. Rev. Lett. **90**, 157203 (2003).
[33] M. T. Glossop, S. Kirchner, J. H. Pixley, and Q. Si, Phys. Rev. Lett. **107**, 076404 (2011).
[34] A. Cai, Z. Yu, H. Hu, S. Kirchner, and Q. Si, Phys. Rev. Lett. **124**, 027205 (2020).
[35] J. L. Smith and Q. Si, Phys. Rev. B **61**, 5184 (2000).
[36] Q. Si and J. L. Smith, Phys. Rev. Lett. **77**, 3391 (1996).
[37] R. Chitra and G. Kotliar, Phys. Rev. Lett. **84**, 3678 (2000).
[38] Q. Si, S. Rabello, K. Ingersent, and J. L. Smith, Nature (London) **413**, 804 (2001).
[39] L. V. Keldysh, Sov. Phys. JETP **20**, 1018 (1965).
[40] A. Kamenev, *Field Theory of Non-Equilibrium Systems* (Cambridge University, Cambridge, 2011).
[41] H. Guo, Y. Gu, and S. Sachdev, Phys. Rev. B **100**, 045140 (2019).
[42] L. Zhu, S. Kirchner, Q. Si, and A. Georges, Phys. Rev. Lett. **93**, 267201 (2004).
[43] S. Kirchner and Q. Si, Phys. Rev. Lett. **103**, 206401 (2009).
[44] M. T. Glossop and K. Ingersent, Phys. Rev. B **75**, 104410 (2007).
[45] Z. Yu, F. Zamani, P. Ribeiro, and S. Kirchner, Phys. Rev. B **102**, 115124 (2020).
[46] S. Kirchner, L. Zhu, Q. Si, and D. Natelson, Proc. Natl. Acad. Sci. USA **102**, 18824 (2005).
[47] H. Shen, P. Zhang, R. Fan, and H. Zhai, Phys. Rev. B **96**, 054503 (2017).